Lei Zhao, Qin Ye, Ke-Li Wu, Geng Chen, and Wenhua Yu

A New High-Resolution Electromagnetic Human Head Model

A useful resource for a new specific-absorption-rate assessment model.

A high-resolution realistic human head model for the human exposure assessment of the specific absorption rate (SAR) is presented in this article. To our best knowledge, this model is the first Chinese electromagnetic (EM) human head model (CMODEL). The model is built using the first Chinese Visible Human (CVH) data set containing 3,640 serial axial anatomical images. In particular, the model has a voxel resolution of $0.16 \times 0.16 \times 0.25\ \mathrm{mm}^3$ for the head part and $0.16 \times 0.16 \times 0.5\ \mathrm{mm}^3$ for the shoulder part. Such a high-resolution model allows for an accurate simulation of 49 different tissues and organs for the SAR assessment. A numerical investigation concerning the detailed SAR distribution of the standard specific anthropomorphic mannequin (SAM) model, the popular but low-resolution HUGO model, and this CMODEL is conducted and involves exposing the three models to radiation from the same dual-band antenna, and this investigation demonstrates the usefulness of a high-resolution EM human head model. For the sake of comparison, the eye models that are extracted from the CMODEL and HUGO models, which are illuminated by a one-half wavelength dipole antenna, are employed to demonstrate the advantage of the CMODEL for the SAR assessment.

Digital Object Identifier 10.1109/MAP.2016.2593966
Date of publication: 23 August 2016

RADIATION AND HUMAN HEALTH

In the past few decades, EM energy absorption through wave-radiation exposure and its effects on the human body has been a tremendous public health concern. Mobile phones that cause EM exposure while being held closely to the human head is one category of concern, and most countries have legally regulated safety guidelines and exposure limits. Many studies have calculated the radio frequency (RF) SAR in a human body exposed to an EM field [1]–[7]. Computational methods for assessing the SAR have also drawn a great deal of attention from international standard committees such as IEEE Standards Coordinating Committees 34 and 28 (ICES), which have accepted the finite-difference time-domain (FDTD) method [8], [9] as a suitable assessment scheme.

Although a computed SAR value is accepted by the EM community, calculated SAR distribution can be uncertain due to a number of factors, including the implementation of numerical algorithms, modeling radiating sources, and human head models. The human head model is the largest cause for result discrepancies in reports produced for any given mobile-phone model and numerical method. In fact, the feature size, number of tissues, and resolution of the model have important roles in SAR calculations. In the late 1970s, the form of the human body was essentially equated to a configuration of homogenous prolate spheroids, ellipsoids, and cylinders. Then, layered tissue models [10] consisting of a few types of tissues with different dielectric properties were used to approximate the human anatomy. By increasing the number of tissue layers, a systematic refinement of the model can be obtained. Recently, a number of realistic partial or whole-body human models have been reported in the literature (see Table 1). BABY and CHILD are the first examples of voxel tomographic models created from computed tomography (CT) data, containing 256 × 256 pixels per slice. BABY consists of 142 slices, and CHILD has 144 slices of images [11]. The German Research Center for Environmental Health is developing a library of voxel phantoms [16], [17], [26], [27]. The most detailed voxel model created to date is the VIP-Man, which was constructed from anatomical data generated from the Visible Human Project (VHP) of the U.S. National Library of Medicine [28]. The color photographs from the VHP have been used to segment approximately 1,400 different structures with a resolution of 0.33 × 0.33 × 1 mm^3 in the VIP-Man model [19]. A few voxel Asian phantoms have also been developed in Japan [20], [22], [24], South Korea [23], [29], [30], and China [25]. The Chinese CNMAN male model [25] was constructed from color photographs of the first CVH data set [31], [32] with a voxel size of 0.16 × 0.16 × 1 mm^3, consisting of 29 tissues or organs for the whole body. All of the aforementioned voxel models were developed and reported for radiation protection purposes. For SAR calculations, a few anatomy voxel models are available in the community. The popular HUGO model [33] with a resolution of 1 × 1 × 1 mm^3 was built based on the VHP data set. The NORMAN model, developed in 1995, was created from a set of magnetic resonance imaging (MRI) scans with a resolution of 2.04 × 2.04 × 1.95 mm^3 and was segmented into 30 different tissue types. Enhanced high-resolution, whole-body human models of the virtual family, available through the Foundation for Research on Information Technologies in Society, consist of four novel anatomical whole-body models [34]. The resolution of the family models is 0.5 × 0.5 × 1 mm^3 for the head and 0.9 × 0.9 × 2 mm^3 for the trunk and limbs.

In this article, we further discuss the development of the CMODEL, which was designed based on the female model in the CVH data set [31], [32]. The applications of the CMODEL and how it may be used for SAR calculations is also numerically explored. Additionally, the images in the CVH data set originate from photos of a milled human specimen, and at a resolution of 3,072 × 2,048 pixels, the images are much clearer than those obtained by using a CT or MRI scan [32].

A NEW HIGH-RESOLUTION MODEL

MODEL DESCRIPTION

We developed the CMODEL at The Third Military Medical University and The Chinese University of Hong Kong [31], [32], having originally based it on the axial anatomical color

TABLE 1. THE EXISTING VOXEL HUMAN MODELS.

Model	Reference and Year	Images	Ethnic Group	In-Plane Resolution (mm^3)	Slice Thickness (mm)	Array Size (pixels/in)	Number of Slices	Number of Tissues
BABY	[11] 1988	CT	Caucasian	0.85 × 0.85	4	256 × 256	142	54
CHILD	[11] 1988	CT	Caucasian	1.54 × 1.54	8	256 × 256	144	64
VoxelMan	[11], [12] 1992	CT	Caucasian	1 × 1	0.5 head, 1.0 body	256 × 256	129	45
NORMAN	[14], [15] 1995	MRI	Caucasian	2.04 × 2.04	1.95	256 × 256	871	37
Golem	[16], [17] 1998	CT	Caucasian	2.08 × 2.08	8	256 × 256	220	29
ADELAIDE	[18] 1999	CT	Caucasian	2.53 × 2.53	10	128 × 128	54	26
VIP-Man	[19] 2000	Color photos	Caucasian	0.33 × 033	1	2,048 × 1,216	1,871	36 body, 20 (24) head
Otoko	[20] 2001	CT	Caucasian	0.98 × 0.98	10	512 × 512	N/A	26 body
UF Newborn	[21] 2002	CT	Caucasian	0.59 × 0.59	1	512 × 512	485	43
UF Two Months	[21] 2002	CT	Caucasian	0.488 × 0.488	1.25	512 × 512	438	43
Nagaoka	[22] 2004	MRI	Japanese	0.9375 × 0.9375 head, 1.875 × 1.875 body	2	256 × 256	866	51
KOR-Man	[23] 2004	MRI/CT	Korean	2 × 2	5	300 × 150	344	29
JM Phantom	[24] 2006	CT	Japanese	0.98 × 0.98	1	512 × 512	N/A	32
CNMAN	[25] 2007	Color photos	Chinese male	0.16 × 0.16	0.5 head, 1.0 body	3,072 × 2,048	1,795	29
CMODEL	[This work] 2008	Color photos	Chinese female	0.16 × 0.16	0.25 head, 0.5 body	3,072 × 2,048	950 head	49 head

CT, computer tomography; MRI, magnetic resonance imaging.

photos of the CVH female data set. To ensure the integrity of the images and to avoid losing fine structures, such as teeth, nasal conchae, and articular cartilage from the milling surface, the photos were taken in a frozen chamber. Two sets of CVH data were produced: one for a male and one for a female. The first CMODEL is based on the CVH female data set obtained by 0.25-mm spacing for the head part and 0.5-mm spacing for rest of the model. There are a total of 3,640 serial slices across the entire body, and each cross-section tag image file format (TIFF) image contains 6,291,456 pixels. Thus, the CMODEL voxel model can provide accurate EM simulation results for SAR assessments. To the best of our knowledge, such a high-resolution head model is the finest virtual human model available for EM simulations to date. Figure 1 shows the three-dimensional (3-D) head model, in which 49 biological tissues can be identified. These biological objects are generated from the segmentation of 950 anatomical cross-sectional images. All of the tissues have been associated to the corresponding EM material characteristics according to published data from the U.S. Federal Communications Commission (FCC) [37], as listed in Table 2.

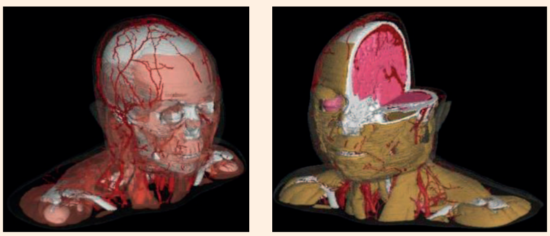

(a) (b)

FIGURE 1. The high-resolution CMODEL head model with a resolution of 0.16 × 0.16 × 0.25 mm^3 for the head part and 0.16 × 0.16 × 0.5 mm^3 for the shoulder part: (a) transparent view and (b) cutting view.

Two major considerations must be taken into account when discretizing an object to be simulated: 1) an accurate description of the detailed physical features and 2) a low numerical dispersion. To maintain a sufficiently low numerical dispersion in numerical simulations, the grid size should be approximately one-tenth of the wavelength. With the largest grid dimension of 0.25 mm in the CMODEL, its highest frequency could be 120 GHz. The transparent cutting view of the computational head model is shown in Figure 2, which includes 15 tissue types.

TABLE 2. THE TISSUES IDENTIFIED IN THE CMODEL AND RELATED TISSUES PROVIDED BY THE FCC.

Number	Tissues Identified in the CMODEL	Tissues Provided by the FCC	Number	Tissues Identified in the CMODEL	Tissues Provided by the FCC
1	Fattiness	Fat (mean)	26	Sinus sagittalis superior	Blood
2	Cancellous bone	Cancellous bone	27	Sinus sagittalis inferior	Blood
3	Cerebral white matter	White matter	28	Sinus transversus left	Blood
4	Cerebral gray matter	Gray matter	29	Sinus transversus right	Blood
5	Hippocampus	Gray matter	30	Sinus rectus	Blood
6	Gyrus dentatus	Gray matter	31	Confluens sinuum	Blood
7	Nucleus caudatus	Gray matter	32	Sinus sigmoideus left	Blood
8	Putamen	Gray matter	33	Sinus sigmoideus right	Blood
9	Globus pallidus	Gray matter	34	Sinus occipitalis	Blood
10	Corpus amygdaloideum	Gray matter	35	Spinal nerves	Nerve (spinal cord)
11	Claustrum	Gray matter	36	Spinal cord	Nerve (spinal cord)
12	Thalamus dorsalis	Gray matter	37	Lens nucleus	Lens nucleus
13	Brain axis	Gray matter	38	Nervus opticus left	Nerve (spinal cord)
14	Substantia nigra left	Gray matter left	39	Nervus opticus right	Nerve (spinal cord)
15	Substantia nigra right	Gray matter right	40	Cartilage	Cartilages
16	Nucleus rubber right	Gray matter	41	Tongue	Tongue
17	Nucleus rubber left	Grey matter	42	Lateral ventriculus	Cerebro spinal fluid
18	Cerebellum	Gray matter	43	Ventriculus tertius	Cerebro spinal fluid
19	Nucleus dentatus left	Gray matter	44	Ventriculus quartus	Cerebro spinal fluid
20	Nucleus dentatus right	Gray matter	45	Septum pellucidum	Cerebro spinal fluid
21	Hypophysis	Gray matter	46	Aqueductus mesencephali	Cerebro spinal fluid
22	Skin	Skin (dry)	47	Canalis centralis	Cerebro spinal fluid
23	Eyeball	Eyeball (sclera)	48	Vitreous body	Vitreous humor
24	Muscle (parallel fiber)	Muscle (parallel fiber)	49	Thyroid thymus	Thyroid thymus
25	Blood vessel	Blood			

FCC: Federal Communications Commission.

IMAGE SEGMENTATION

The most difficult steps toward obtaining computer-usable EM human models are the segmentation and classification of the raw image data. The first CMODEL was built by segmenting the TIFF-formatted images of the CVH female model cross section by cross section and manually identifying all of the visible biological tissues. In the segmentation procedure, if errors are made while processing the raw data that was collected from the CVH data set, then the errors must be corrected by operators who have thorough anatomical knowledge and who are extensively familiar with the CVH data set. By using a hybrid segmentation procedure of computer vision and manual intervention, the various anatomical tissues and organs can be accurately identified. For organs that are not easily distinguished, manual intervention is necessary. Due to the complexity and

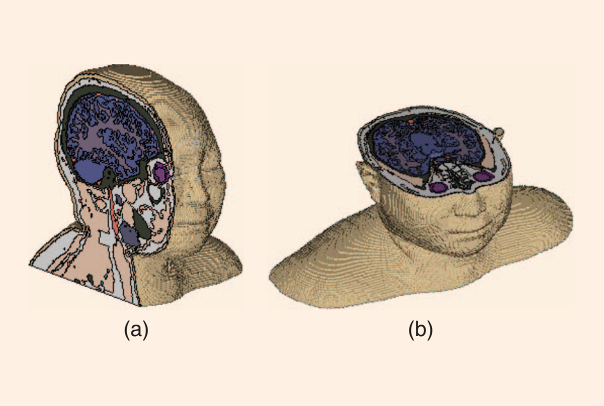

FIGURE 2. Cutting views of the CMODEL with the detailed features: (a) vertical and (b) horizontal cutting planes.

intensiveness of the head structure, the segmentation with manual intervention was very involved. As an example, an original image and its segmented image are shown in Figure 3(a) and (b), respectively. It is obvious that the manually segmented photograph in Figure 3(b) has a clear boundary compared to the original.

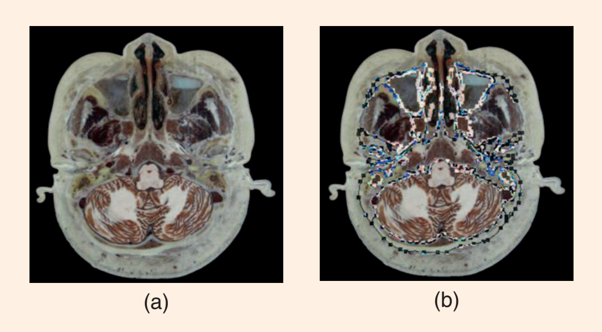

FIGURE 3. Color photographs before and after segmentation: (a) the original transversal photograph and (b) the same slice after segmentation.

IDENTIFICATION PROCESS

When identifying the distinct biological tissues, efficient path selection tools must be used. After the tissue paths are drawn, black and white colors are added to the images, and they are exported in the binary image format. Once the binary images are obtained, each identified tissue is filled with a single color. In the filling process, some errors such as a wrong path attribute and an overlap between two segmented regions may occur. Therefore, the preliminary fillings need to be carefully verified and amended by comparing the preliminary filling results with the initial segmented image. Figure 4 illustrates the filling procedure.

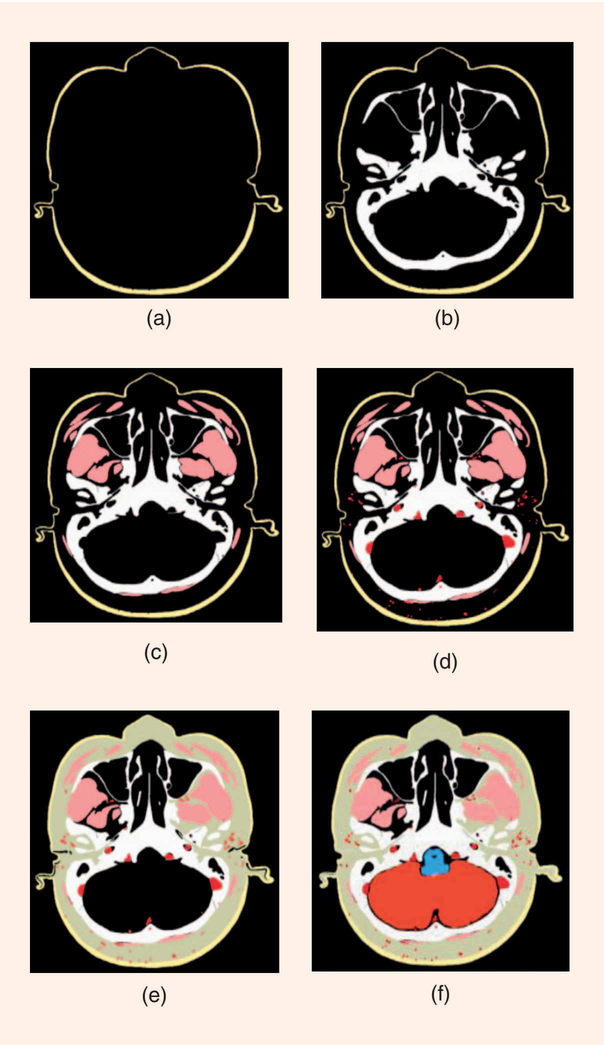

FIGURE 4. A filling procedure with different colors for different tissues: (a) one tissue, (b) two tissues, (c) three tissues, (d) four tissues, (e) five tissues, and (f) all tissues.

MODEL VALIDATION

To verify the physical objects, a 3-D visualization tool validates the assembly of the 2-D images by using them to generate a 3-D model, which is done by converting the transverse images into sagittal images. For the head model, 950 transverse images were converted into sagittal images, as shown in Figure 5. From the sagittal images based on the preliminary segmentation images, some saw-tooth-like

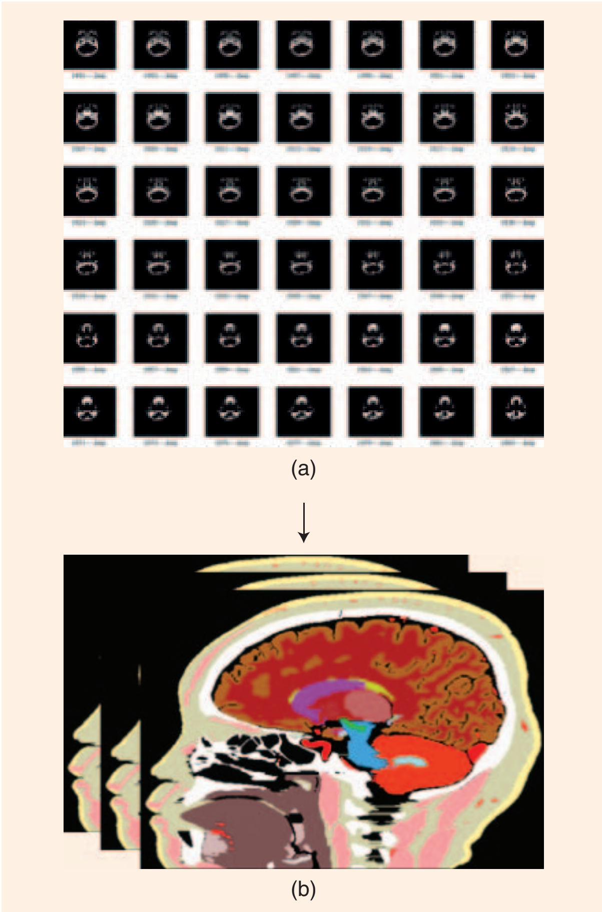

FIGURE 5. The procedure demonstration to convert horizontal images into sagittal images: (a) horizontal section images and (b) sagittal images.

boundary contours were found in many tissues. To ensure a high-precision model, the preliminary segmentation results must be amended manually. Such a validation procedure has been done in the coronal section images as well, which assures that the model is accurate with realistic boundary surfaces. To demonstrate the rich information of the anatomical structure in the high-resolution CMODEL, the details of the tissues around an eye are shown in Figure 6, where 15 anatomic objects are identified.

To compare with the high-quality CMODEL, we plotted the 3-D models of one eye extracted from both the CMODEL [Figure 7(a)] and the HUGO [Figure 7(b)] model. There is no question that a SAR assessment of the CMODEL will generate more reliable results. We also show the ear and skin difference in the CMODEL [Figure 8(a)] and the HUGO model [Figure 8(b)], which has an important role in a SAR assessment.

SAR ASSESSMENT

To demonstrate the usefulness of the high-resolution human model, we conducted a comparison study of the calculation of the SAR distribution for three different head models: homogeneous SAM, HUGO, and CMODEL. To maintain reasonable accuracy for results that were generated using an ordinary computer facility, a cell dimension of 2 mm was first tested. Having set the required resolution, a coarse head model with a spatial resolution of $1.34 \times 1.38 \times 2$ mm^3 could be extracted from the CMODEL, which was then prepared for calculating the SAR distribution caused by a mobile-phone antenna in close vicinity. The antenna is shown in Figure 9(a) and is located 1.5 cm away from the head model. The EM properties (ε_r and σ) of 15 major tissues in the model can be obtained from FCC published data [35]. The properties of the other 34 tissues were replaced with similar tissues, as listed in Table 2.

The mobile-phone antenna in this study was a dual-band planar inverted-F antenna (PIFA), as shown in Figure 9(b). The antenna structure of $14 \times 40 \times 100$ mm^3 was built on an FR4 substrate ($\varepsilon_r = 4.9, \sigma = 0.025$ S/m). The dual-band antenna works at the global system for the mobile communications band (900 MHz) and the digital cellular system band (1,800 MHz). The simulated return loss is shown in Figure 9(c).

For all of the following examples, the computational domain includes the model with a white space of 20 cells between the model and domain boundary, without special mention. The convolutional perfectly matched layer [36]–[38] is used to truncate the computational domain. The mesh size is selected to be same size as the voxel resolution, and the modulated Gaussian pulse is used to excite the dipole antenna in the FDTD simulations. The simulations were carried on a computer cluster that included 30 compute nodes (a total of 60 Intel Xeon E5-2680 central processing units and 7,680 GB of random access memory) connected using a 10-GB/s high-speed network.

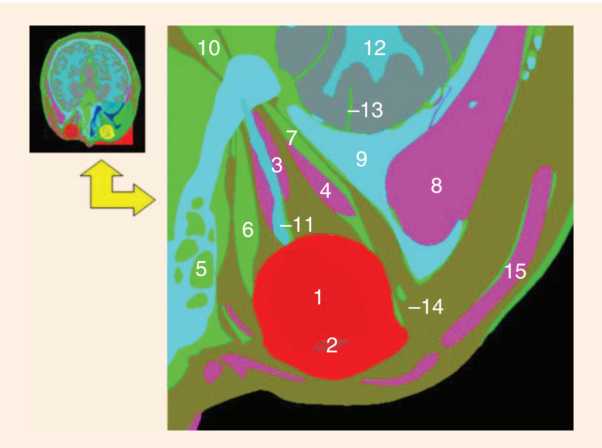

FIGURE 6. The image in the upper left-hand corner is one CMODEL cross section, and the right-hand image is the zoomed localized area including one eye. The tissues around the eyeball include region 1: eyeball; region 2: lens; region 3: inferior rectus; region 4: external rectus muscle; region 5: ethmoid bone; region 6: internal rectus muscle; region 7; musculus obliquus superior; region 8: temporalis; region 9: greater wing of sphenoid bone; region 10: orbital gyri; region 11: optic nerve; region 12: temporal lobe; region 13: lacuna between tissues; region 14: tarsal plate; and region 15: buccinators.

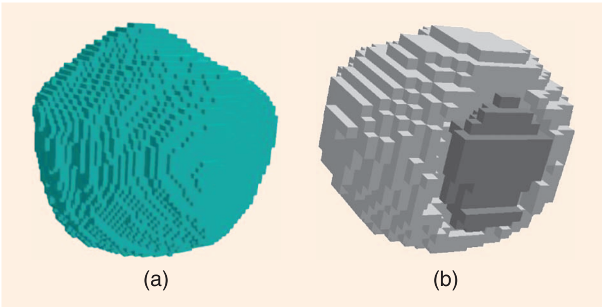

FIGURE 7. The eye models extracted from (a) the CMODEL and (b) the HUGO model.

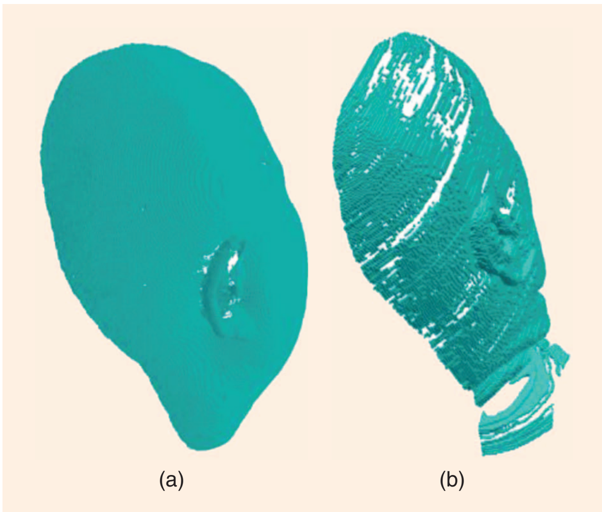

FIGURE 8. An ear with partial skin models extracted from (a) the CMODEL and (b) the HUGO model.

For a fair comparison, the total radiated power for each case was set at 1 W. The SAR distribution is defined by

$$\mathrm{SAR} = \frac{\sigma |\bar{E}|^2}{\rho}, \qquad (1)$$

where $\bar{E}$ is the computed electric field strength at a given frequency and location, σ is the local conductivity inside the head models, and ρ is the local density of the head tissue. Averaged SAR distributions of 1 and 10 g were obtained by integrating (1) over a specified volume of a cube and normalizing to 1 and 10 g. Table 2 lists calculated maximum SAR values using the head models SAM, HUGO, and the CMODEL. All models were illuminated by the same PIFA at frequencies of 900 and 1,800 MHz, respectively. The averaged 10-g SAR distributions at 900 MHz of the SAM, HUGO, and CMODEL head models are shown in Figures 10–12, respectively. The cut plane that contained the maximum average SAR was chosen for each model. The discrepancy of the distributions concerning the averaged SAR values over 1 and 10 g of tissues shows the necessity for using high-resolution anatomy models for realistic simulations.

The discrepancy of the distributions concerning the averaged SAR values over 1 and 10 g of tissues shows the necessity for using high-resolution anatomy models for realistic simulations.

With the object-oriented CMODEL, the field distribution over a specific object can be investigated. In Figure 13, (a) shows the 10-g averaged SAR distribution on the surface of the bones, and (b) presents the 10-g

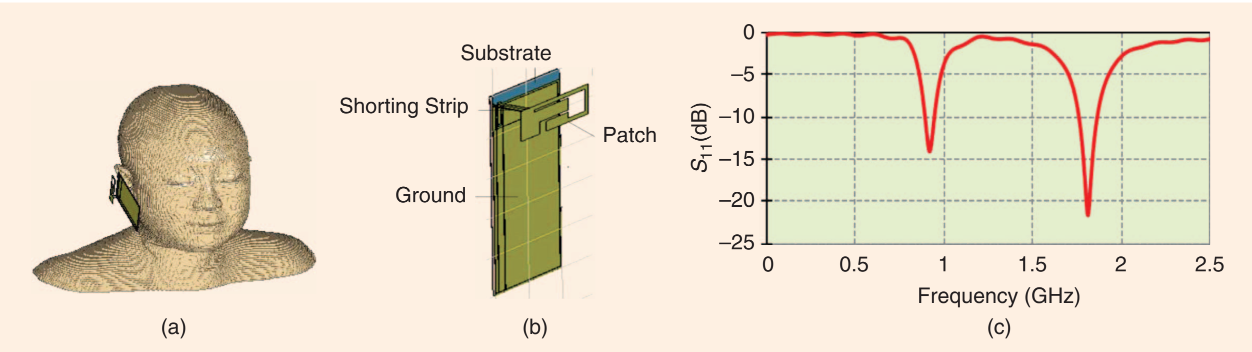

FIGURE 9. The CMODEL with a PIFA mobile antenna: (a) the CMODEL with the PIFA antenna near the ear, (b) the PIFA antenna configuration, and (c) the return loss of the PIFA antenna.

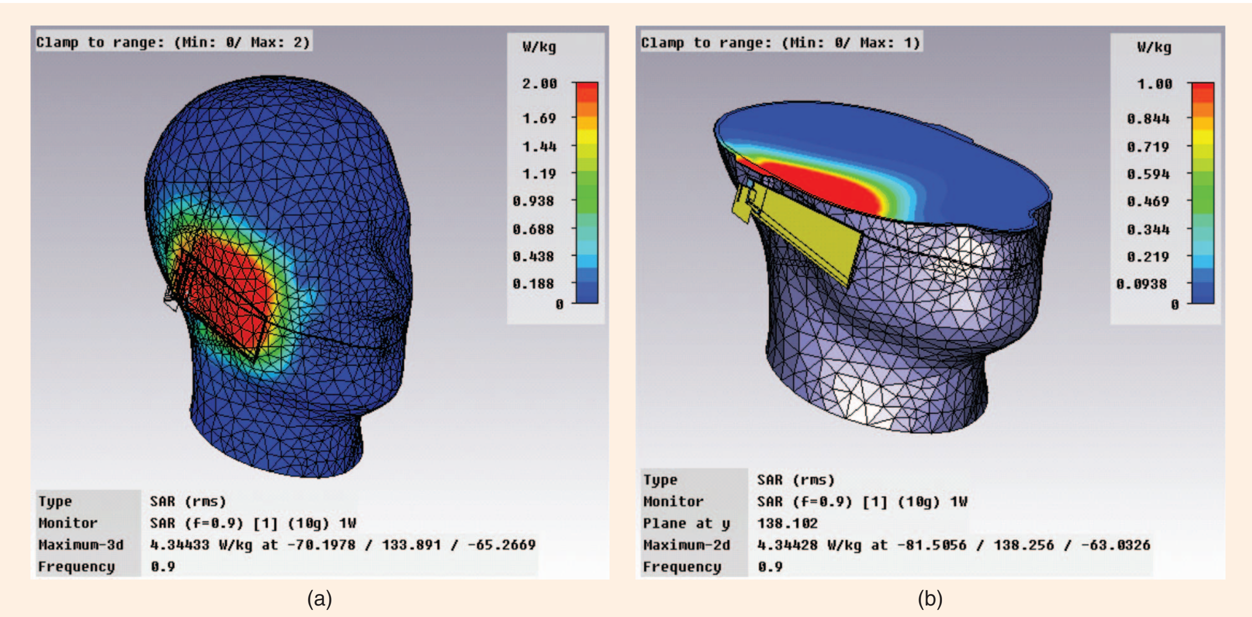

FIGURE 10. The 10-g averaged SAR distributions in the SAM model at 900 MHz: (a) the 3-D surface SAR distribution and (b) the 2-D SAR distribution in a cutting plane.

averaged SAR distribution on muscle tissues. Generally speaking, the high-resolution CMODEL can be used to calculate the detailed SAR distribution and the induced temperature change within the certain tissues of interest.

Today, more focus is given to simulations that demonstrate the effects of RF radiation on more sensitive organs that are located much closer to the working antenna, such as the eyes. The eye models extracted from the CMODEL and the HUGO human head model were used to investigate the SAR values for eyes that are exposed to a dipole antenna operating at 28 GHz, which is commonly used in fifth-generation communication systems. The distance between the eye model and the one-half-wavelength dipole antenna is 2 mm. Figure 14 shows the 1-g averaged SAR distribution over the eye model. The 1-g averaged SAR distributions at 28 GHz on a cutting plane in the CMODEL

Today, more focus is given to simulations that demonstrate the effects of RF radiation on more sensitive organs that are located much closer to the working antenna, such as the eyes.

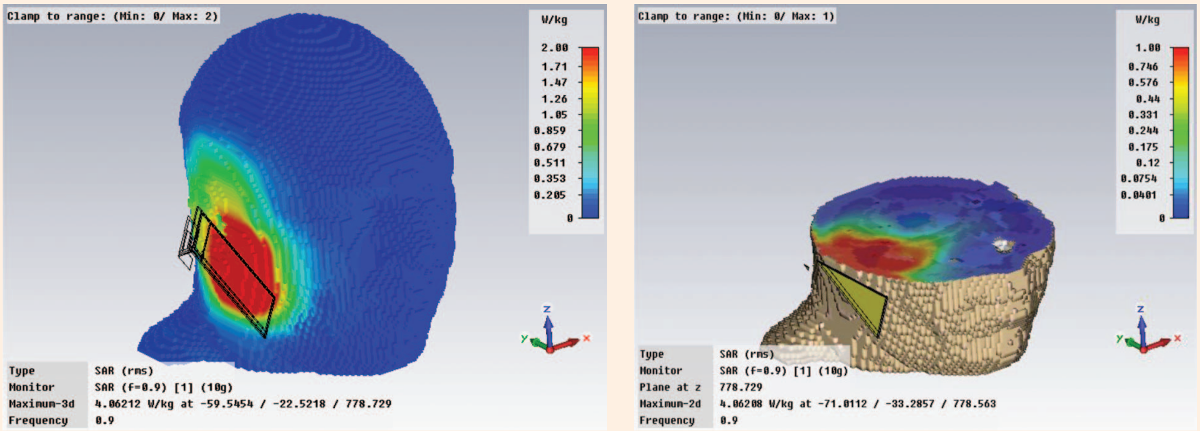

(a) (b)

FIGURE 11. The 10-g averaged SAR distributions in the HUGO model: (a) the 3-D surface SAR distribution and (b) the 2-D SAR distribution in one cross section.

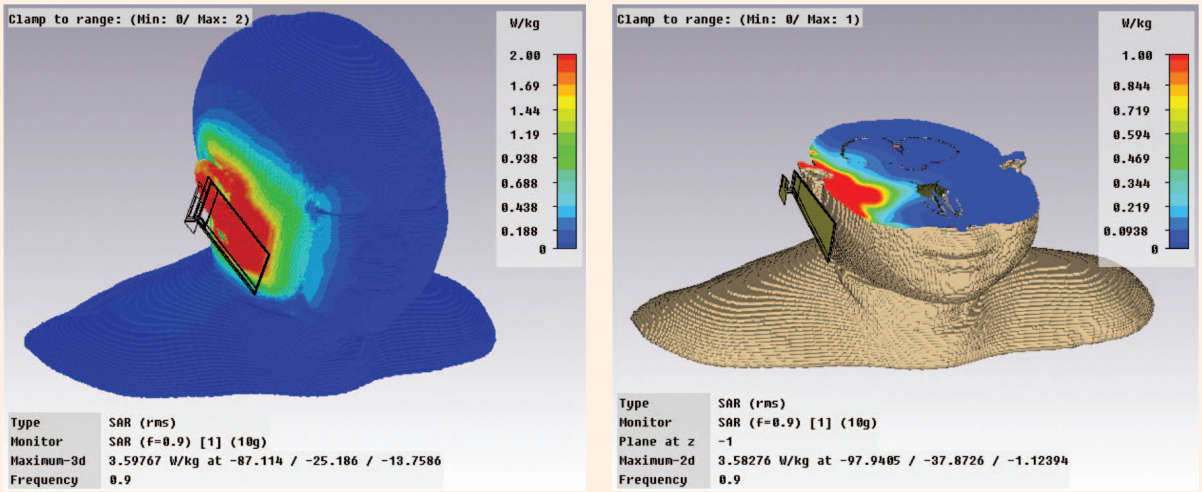

(a) (b)

FIGURE 12. The 10-g averaged SAR distributions in the CMODEL at 900 MHz: (a) the 3-D surface SAR distribution and (b) the SAR distribution in one cutting plane.

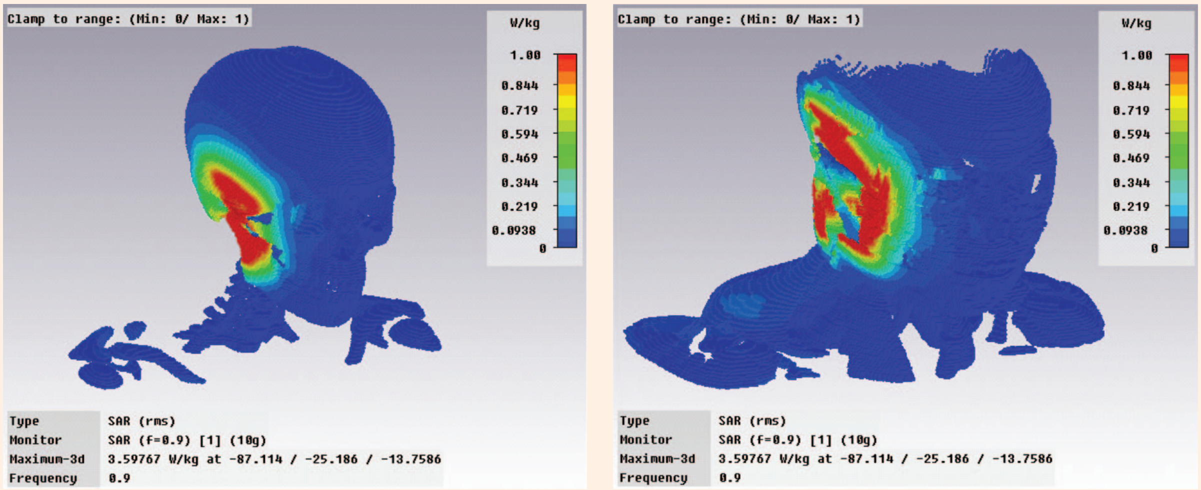

(a) (b)

FIGURE 13. The 10-g averaged SAR distributions at 900 MHz in the CMODEL: in (a) bones and (b) muscle tissue.

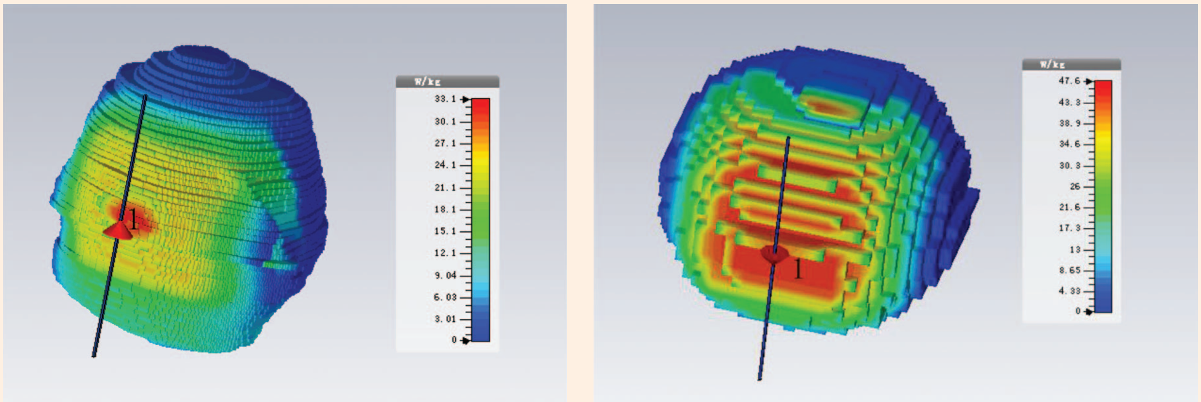

(a) (b)

FIGURE 14. The 1-g averaged SAR distributions at 28 GHz in human eye models: (a) the CMODEL and (b) the HUGO eye models.

and the HUGO model are plotted in Figure 15(a) and (b), respectively.

To compare the difference between the CMODEL and the HUGO model illuminated by a one-half-wavelength dipole antenna for the SAR assessment, we calculated the 1-g peak SAR in the setting of Figure 14(a) and (b). The 1-g peak SAR inside the HUGO model and CMODEL at frequencies of 27, 27.5, 28, 28.5, and 29 GHz are summarized in Figure 16.

CONCLUSIONS

This article describes a high-resolution human head model (CMODEL) with a resolution of 0.16 × 0.16 × 0.25 mm^3 for the head and 0.16 × 0.16 × 0.5 mm^3 for the shoulder. A human model with 49 tissue types can be used for SAR assessment as well as for general purposes. The electric properties of tissues in the CMODEL are same as those published by the FCC for SAR assessment. A comparison of SAR distributions over the CMODEL with the standard SAM model and the popular HUGO model was investigated. The eye models extracted from CMODEL and HUGO model were also investigated to compare SAR assessments. The results demonstrate that the new high-resolution head model has advantages over existing models for accurate SAR assessments.

ACKNOWLEDGMENTS

Lei Zhao thanks Prof. Pheng Ann Heng and Dr. Yongming Xie of the Department of Computer Science and Engineering at The Chinese University of Hong Kong for their contributions to CMODEL processing. This work was supported in

The results demonstrate that the new high-resolution head model has advantages over existing models for accurate SAR assessments.

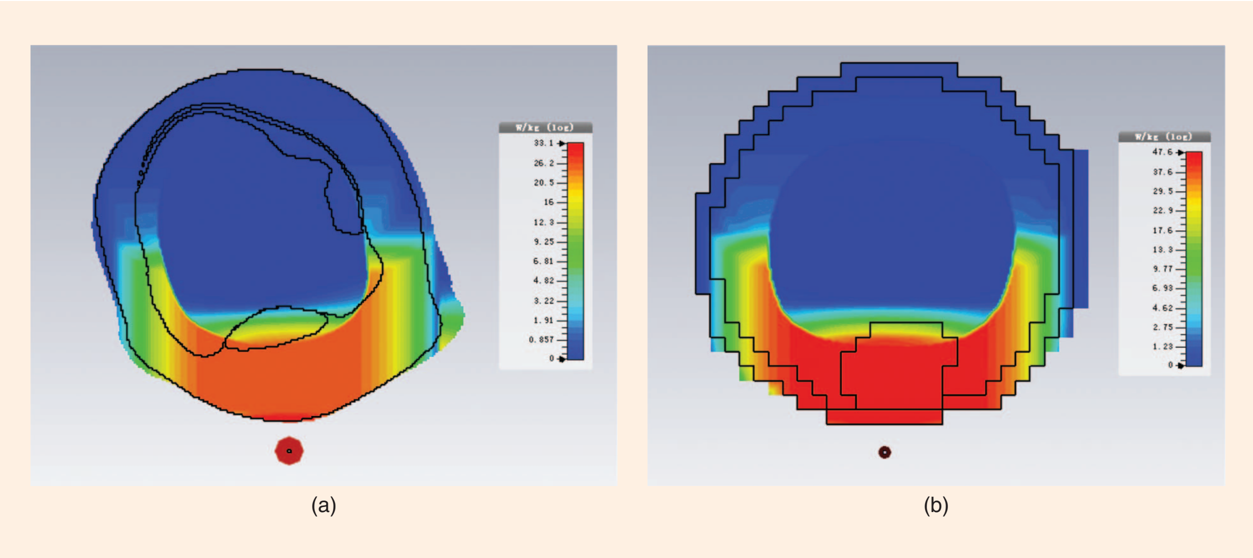

FIGURE 15. The 1-g averaged SAR distributions at 28 GHz on one cutting plane: in (a) the CMODEL and (b) the HUGO eye models.

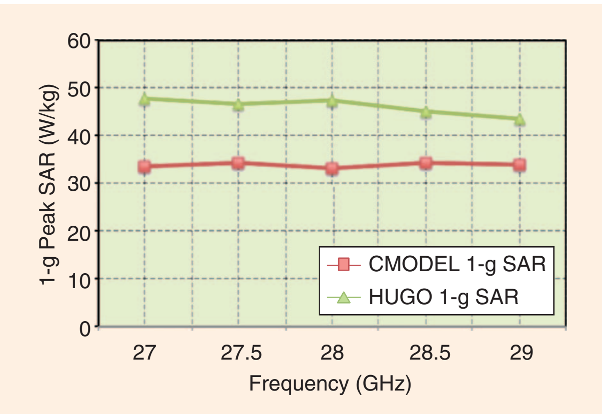

FIGURE 16. The 1-g peak SAR variation in the CMODEL and HUGO eye models, with frequencies from 27 to 29 GHz.

part by the Shun Hing Institute of Advanced Engineering, The Chinese University of Hong Kong, the National Science Foundation of China under grant 61372057, the Natural Science Foundation of the Jiangsu Normal University under grant 11XLR25, and the Postgraduate Innovation Project of Jiangsu Province under grant CXZZ13 0973.

AUTHOR INFORMATION

Lei Zhao (leizhao@jsnu.edu.cn) serves as the director of the Center for Computational Science and Engineering as well as associate dean at its School of Mathematics and Statistics, both of Jiangsu Normal University, China. His current research interests include computational electromagnetics, electromagnetic radiation to the human body, simulation and design of antennas, and numerical methods for partial differential equations.

Qin Ye (yeqin@jsnu.edu.cn) has been with the School of Biology of Jiangsu Normal University, China, since 1998. During 2013–2014, she was a visiting scholar at the Karmanos Cancer Center in Michigan. Her current research interests include the molecular mechanism of aberrant epigenetic modification and electromagnetic radiation to the human body.

Ke-Li Wu (klwu@ee.cuhk.edu.hk) has been with The Chinese University of Hong Kong, where he has served as a professor and director of the Radio Frequency Radiation Research

Laboratory since 1993. His current research interests include partial element equivalent circuits and physics-based model order reduction for electromagnetic modeling of high-speed circuits, antennas for wireless terminals, low-temperature cofired ceramic-based multichip modules, and radio-frequency identification technologies.

Geng Chen (gengchn@163.com) is currently a visiting student at the the Center for Computational Electromagnetics of the University of Illinois, Urbana-Champaign. His research interests include computational electromagnetic methods, parallel processing techniques, numerical methods, and software development.

Wenhua Yu (wenyu@2comu.com) currently serves as both a visiting professor at Jiangsu Normal University, China, and director of the Jiangsu Big Data Key Lab for Education Science and Engineering. His current research interests include big data techniques, computational electromagnetic methods, software development techniques, parallel processing techniques, hardware acceleration techniques, and simulation and design of antennas, antenna arrays, and microwave circuits. He is a Senior Member of the IEEE.

REFERENCES

[1] A. Schiavoni, P. Bertotto, G. Richiardi, and P. Bielli, "SAR generated by commercial cellular phones-phone modeling, head modeling, and measurements," *IEEE Trans. Microwave Theory Tech.*, vol. 48, no. 11, pp. 2064–2071, Nov. 2000.

[2] O. Gandhi, G. Lazzi, and C. Furse, "Electromagnetic absorption in the human head and neck for mobile telephones at 850 and 1900 MHz," *IEEE Trans. Microwave Theory Tech.*, vol. 44, no. 10, pp. 1884–1897, Oct. 1996.

[3] G. Lazzi and O. P. Gandhi, "Realistically tilted and truncated anatomically based models of the human head for dosimetry of mobile telephones," *IEEE Trans. Electromagn. Compat.*, vol. 39, no. 1, pp. 55–61, Feb. 1997.

[4] A. Lee, H. Choi, and J. Choi, "Study on SARs in head models with different shapes by age using SAM model for mobile phone exposure at 835 MHz," *IEEE Trans. Electromagn. Compat.*, vol. 49, no. 2, pp. 302–312, May 2007.

[5] Q. Li and O. Gandhi, "Thermal implications of the new relaxed IEEE RF safety standard for head exposures to cellular telephones at 835 and 1,900 MHz," *IEEE Trans. Microwave Theory Tech.*, vol. 54, pp. 3146–3154, July 2006.

[6] A. Rodrigues, L. Malta, J. Viana, L. Rodrigues, and J. Ramirez, "A head model for the calculation of SAR and temperature rise induced by cellular phones," *IEEE Trans. Magn.*, vol. 44, no. 6, pp. 1446–1449, June 2008.

[7] C. Durney, "The physical interactions of radiofrequency radiation fields and biological systems," *AGARD Lecture Series*, vol. 138, pp. 2.1–2.19, 1985.

[8] W. Yu, R. Mittra, and Y. Liu, *Electromagnetic Simulation Techniques Based FDTD Methods*. Hoboken, NJ: Wiley, 2009.

[9] W. Yu, R. Mittra, and T. Su, *Parallel Finite Difference Time Domain Method*. Norwood, MA: Artech House, 2006.

[10] S. Gutschling and T. Weiland, "Resonance effects inside a human head exposed to a cellular phone," in *Proc. 3rd Int. Conf. Computation in Electromagnetics*, Bath, United Kingdom, pp. 62–66, 1996.

[11] M. Zankl, R. Veit, G. Williams, K. Schneider, H. Fendel, N. Petoussi, and G. Drexler, "The construction of computer tomographic phantoms and their application in radiology and radiation protection," *Radiat. Environ. Biophys.*, vol. 27, no. 2, pp. 153–164, June 1988.

[12] G. Zubal, C. Harrell, E. Smith, Z. Ratner, G. Gindi, and P. Hoffer, "Computerised three-dimensional segmented human anatomy," *Med. Phys.*, vol. 21, no. 2, pp. 299–302, 1994.

[13] G. Zubal and C. Harrel, "Voxel based Monte Carlo calculations of nuclear medicine images and applied variance reduction techniques," *Image Vision Comput.*, vol. 10, no. 6, pp. 342–348, July–Aug. 1992.

[14] D. Jones, "A realistic anthropomorphic phantom for calculating organ doses arising from external photon irradiation," *Radiat. Prot. Dosim.*, vol. 72, no. 1, pp. 21–29, July 1997.

[15] P. Dimbylow, "FDTD calculations of the whole-body averaged SAR in an anatomically realistic voxel model of the human body from 1 MHz to 1 GHz," *Phys. Med. Biol.*, vol. 42, no. 3, pp. 479–490, Mar. 1997.

[16] N. Petoussi-Henss and M. Zankl, "Voxel anthropomorphic models as a tool for internal dosimetry," *Radiat. Prot. Dosim.*, vol. 79, no. 1–4, pp. 415–418, 1998.

[17] M. Zankl and A. Wittmann, "The adult male voxel model 'Golem' segmented from whole-body CT patient data," *Radiat. Environ. Biophys.*, vol. 40, no. 2, pp. 153–162, June 2001.

[18] M. Caon, G. Bibbo, and J. Pattison, "An EGS4-ready tomographic computational model of a fourteen year-old female torso for calculating organ doses from CT examinations," *Phys. Med. Biol.*, vol. 44, no. 9, pp. 2213–2225, Sept. 1999.

[19] X. G. Xu, T. C. Chao, and A. Bozkurt, "VIP-MAN: An image based whole-body adult male model constructed from color photographs of the Visible Human Project for multi-particle Monte Carlo calculations," *Health Phys.*, vol. 78, no. 5, pp. 476–486, May 2000.

[20] K. Saito, A. Wittmann, S. Koga, Y. Ida, T. Kamei, J. Funabiki, and M. Zankl, "Construction of a computed tomographic phantom for a Japanese male adult and dose calculation system," *Radiat. Environ. Biophys.*, vol. 40, no. 1, pp. 69–75, Mar. 2001.

[21] J. Nipper, J. Williams, and W. Bolch, "Creation of two tomographic voxel models of paediatric patients in the first year of life," *Phys. Med. Biol.*, vol. 47, no. 17, pp. 3143–3164, Aug. 2002.

[22] T. Nagaoka, S. Watanabe, K. Sakurai, E. Kuneida, S. Watanabe, M. Taki, and Y. Yamanka, "Development of realistic high-resolution whole-body voxel models of Japanese adult male and female of average height and weight, and application of models to radio-frequency electromagnetic-field dosimetry," *Phys. Med. Biol.*, vol. 49, no. 1, pp. 1–15, Jan. 2004.

[23] C. Lee, J. Lee, and C. Lee, "Korean adult male voxel model KORMAN segmented from magnetic resonance images," *Med. Phys.*, vol. 31, no. 5, pp. 1017–1022, May 2004.

[24] K. Sato, H. Noguchi, K. Y. Emoto, and K. Saito, "Japanese adult male voxel phantom constructed on the basis of CT images," *Radiat. Prot. Dosim.*, vol. 123, no. 3, pp. 337–344, Aug. 2007.

[25] B. Zhang, J. Ma, L. Liu, and J. Cheng, "CNMAN: A Chinese adult male voxel phantom constructed from color photographs of a visible anatomical data set," *Radiat. Prot. Dosim.*, vol. 124, no. 2, pp. 130–136, May 2007.

[26] N. Petoussi-Henss, M. Zankl, U. Fill, and D. Regulla, "The GSF family of voxel phantoms," *Phys. Med. Biol.*, vol. 47, no. 1, pp. 89–106, Jan. 2002.

[27] U. Fill, M. Zankl, N. Petoussi-Henss, M. Siebert, and D. Regulla, "Adult female voxel models of different stature and photon conversion coefficients for radiation protection," *Health Phys.*, vol. 86, no. 3, pp. 253–272, Mar. 2004.

[28] M. Ackerman, "Viewpoint: The visible human project," *J. Biocommun.*, vol. 18, no. 2, p. 14, 1991.

[29] C. Lee, C. Lee, S. Park, and J. Lee, "Development of the two Korean adult tomographic computational phantoms for organ dosimetry," *Med. Phys.*, vol. 33, no. 2, pp. 380–390, Feb. 2006.

[30] S. Park, J. Lee, and C. Lee, "Development of a Korean adult male computational for internal dosimetry calculation," *Radiat. Prot. Dosim.*, vol. 121, no. 3, pp. 257–264, Dec. 2006.

[31] S. Zhang, P. Heng, Z. Liu, L. Tan, M. Qiu, Q. Li, R. Liao, K. Li, G. Cui, Y. Guo, and Y. Xie, "Chinese visible human data sets and their applications," in *First Int. Conf. Digital Human Modeling*, Beijing, China, pp. 530–535, 2007.

[32] S. X. Zhang, P. A. Heng, and Z. J. Liu, "Chinese visible human project," *Clin. Anat.*, vol. 19, no. 3, pp. 204–215, Feb. 2006.

[33] P. Bernardi, M. Cavagnaro, S. Pisa, and E. Piuzzi, "Specific absorption rate and temperature increases in the head of a cellular-phone user," *IEEE Trans. Microwave Theory Tech.*, vol. 48, no. 7, pp. 1118–1126, July 2000.

[34] IT'IS Foundation, Zurich, Switzerland. [Online]. Available: http://www.itis.ethz.ch/index/index_humanmodels.html

[35] Federal Communications Commission, Washington, DC. [Online]. Available: https://www.fcc.gov/general/body-tissue-dielectric-parameters#block-menu-block-4

[36] J. Berenger, "A perfectly matched layer for the absorption of electromagnetic waves," *J. Comput. Phys.*, vol. 114, no. 2, pp. 185–200, Oct. 1994.

[37] S. Gedney, "An anisotropic perfectly matched layer-absorbing medium for the truncation of FDTD Lattices," *IEEE Trans. Antennas Propagat.*, vol. 44, no. 12, pp. 1630–1639, Dec. 1996.

[38] J. Roden and S. Gedney, "Convolution PML (CPML): An efficient FDTD implementation of the CFS–PML for arbitrary media," *Microwave Opt. Technol. Lett.*, vol. 27, no. 5, pp. 334–339, Oct. 2000.